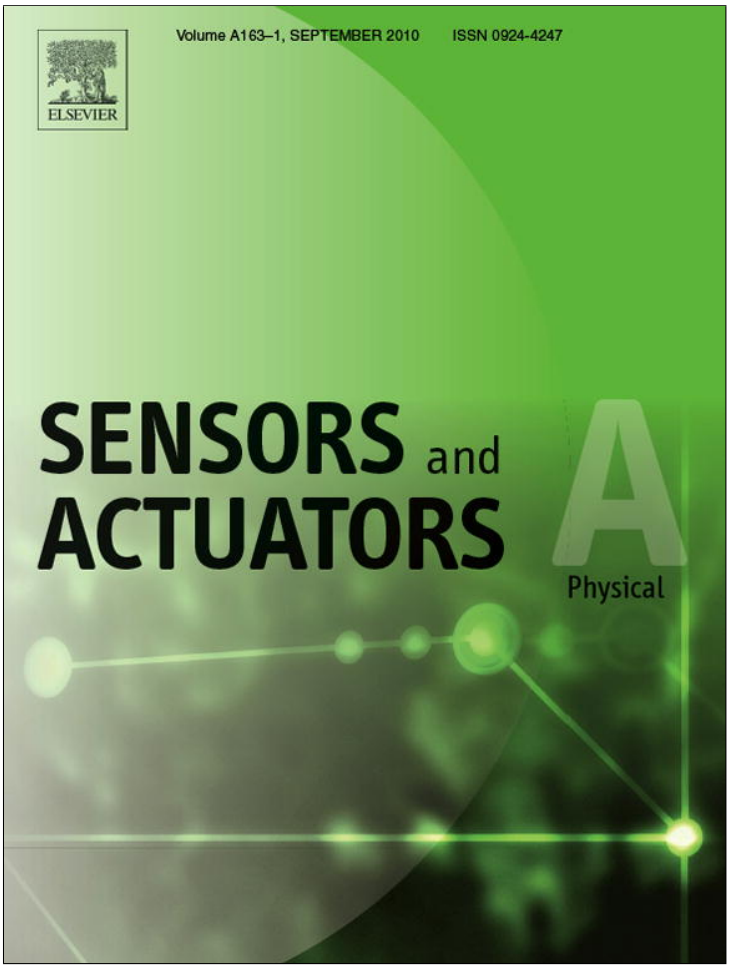

Sensors and Actuators A 163 (2010) 15–24

Contents lists available at ScienceDirect

Sensors and Actuators A: Physical

journal homepage: www.elsevier.com/locate/sna

Thin-Film Detector System for Internal Magnetic Resonance Imaging

R.R.A. Syms [a,*], I.R. Young [a], M.M. Ahmad [a], M. Rea [b], C.A. Wadsworth [c], S.D. Taylor-Robinson [c]

[a] Optical and Semiconductor Devices Group, EEE Department, Imperial College London, Exhibition Road, London SW7 2AZ, UK
[b] Department of Radiology, Imperial College NHS Trust, Praed St., Paddington, London, W2 1NY, UK
[c] Liver Unit, Division of Diabetes Endocrinology and Metabolism, Department of Medicine, Imperial College London, Praed St., Paddington, London, W2 1NY, UK

ARTICLE INFO

Article history:
Received 29 January 2010
Received in revised form 13 May 2010
Accepted 13 May 2010

Keywords:
Microcoil
Flexible coil
Microstrip
Magnetic resonance imaging

ABSTRACT

A detector for *in vivo* internal magnetic resonance imaging (MRI) is demonstrated based on a thin-film RF resonator and a thin-film cable. Each component is constructed on a flexible sheet and mounted on the outside of a catheter, leaving its internal lumens free for clinical use. Space constraints require the sheet to be extremely thin (< 100 μm). Cable formats are compared, and thin-film cables with ≈ 50 Ω impedance at low frequency are formed as a microstrip with a periodically patterned ground, using copper conductors on polyimide substrates. Resonant detectors are also formed on polyimide from multi-turn electroplated copper coils and integrated parallel plate capacitors, which use the substrate as an interlayer dielectric. Methods are developed for obtaining capacitor values for matching and tuning, and compensating for loading. The detector and cable are linked to form a two-metre-long printed detection system and ^{1}H MRI is demonstrated at 1.5 T using *in vitro* liver tissue.

1. Introduction

Small resonant RF detectors have many applications for *in vivo* internal magnetic resonance imaging (MRI), for example for rectal, biliary and arterial imaging. Although small coils generally have low Q factors, this disadvantage is mitigated by the increase in signal-to-noise ratio obtained from close coupling to the signal source [1]. Suitable coil arrangements include single-or multi-turn loops [2–4], parallel conductor transmission lines [5] and opposed solenoids [6,7], constructed by hand winding or from rigid printed circuit boards (PCBs). Compact alternatives for vascular imaging include the loopless catheter antenna [8]. A similar range of coils has been used for catheter tracking [9,10].

In each case, the need for matching and tuning has limited widespread application. Several well-known circuits (for example, shunt or series capacitive matching) may be used. Unfortunately, despite advances in modelling methods that allow 3D coils, skin effects and material losses, it is difficult to estimate coil inductance and resistance accurately. Consequently, capacitor values must be determined experimentally. Multiple capacitors may be needed, and circuits may be re-soldered many times. The end product is acceptable for large coils, but cannot achieve the low cost, small form factor and reproducibility needed for mass deployment. One alternative is to locate the components remotely, using a λ/2 length of cable [11]. However, the strategy is difficult to implement with long catheters.

Microfabrication can improve the situation, since it yields repeatable inductance and resistance. Electroplated spiral coils have been formed on GaAs [12,13], Si [14,15] and glass [16,17]. Microfabricated Helmholtz coils have been constructed [18,19], solenoids have been fabricated on capillaries [20–22], planar coils have been integrated with microfluidics [23,24], and pre-amplifiers have been incorporated [25–27]. More recently, attention has turned to flexible plastics such as polyimide and polyether-ether-ketone [28] and polytetrafluoroethylene [29], which are more suitable for *in vivo* use. Some attempts have been made to integrate capacitors, using coplanar electrodes [30] or double-layer windings [31]. However, no convincing solution to matching has been demonstrated.

We ourselves have demonstrated high-resolution MRI using catheter-mounted flexible microfabricated coils with discrete capacitors [32]. The target application was an endoscopically delivered detector for *in vivo* imaging of the bile duct, with the aim of early detection of cholangiocarcinoma. Because operable tumours must typically be less than1 mm in size, imaging must be carried out with sub-millimetre resolution. The length and diameter of the common bile duct range from 5-10 cm and from 3-8 mm, respectively; however, the duct is normally heavily constricted near any lesion. A 60 mm long coil capable of mounting on an 8 Fr (2.7 mm dia) catheter was developed, which did indeed have suitable resolution.

However, in addition to the matching difficulties described above, little attention was paid to clinical use. For example, the

* Corresponding author. Tel.: +44 207 594 6203.
E-mail address: r.syms@imperial.ac.uk (R.R.A. Syms).

0924-4247/$ – see front matter © 2010 Elsevier B.V. All rights reserved.
doi:10.1016/j.sna.2010.05.017

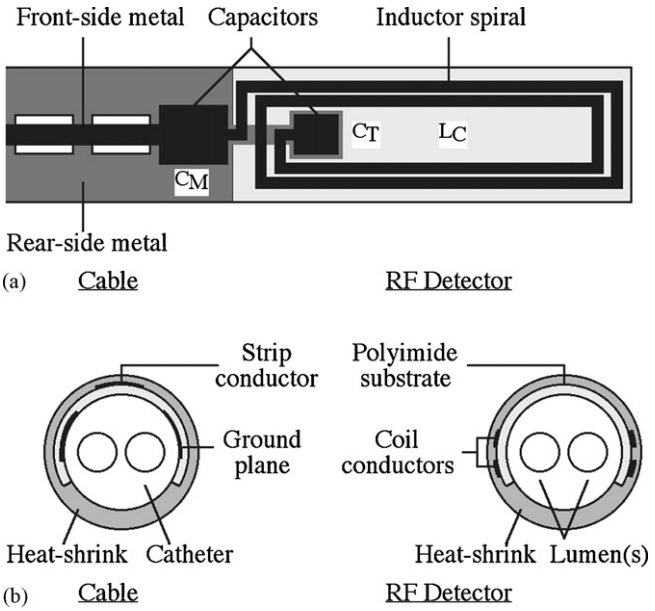

Figure 1. Thin film RF detection system: a) plan view and b) integration on catheter.

capacitors were vulnerable to mechanical damage in a side-opening gastroscope, and the need for joints made it difficult to seal the assembly for use in a wet environment. The sub-miniature coaxial cable used to transmit the detected signal back along the catheter blocked one of the internal lumens, which are typically required for use with a guide-wire or an actuation wire or for injection of contrast agent.

In this paper, we attempt to provide a solution in the form of a thin-film detector with integrated shunt matching capacitors and a thin-film output cable as shown in Figure 1a. The whole structure may be fabricated lithographically from non-magnetic materials and wrapped around a catheter as shown in Figure 1b, avoiding the need for additional components, simplifying sealing and leaving the catheter free for its original use. Except near the coil ends, the configuration is similar to a two-turn planar coil with stacked windings, with a corresponding field of view. The target application here is biliary imaging, which may require data to be acquired for lengths 50–60 mm along the duct. Similar approaches could be used for vascular imaging.

Operation of the system is shown in the equivalent circuit of Figure 2a. Here, a source V_S representing the signal induced by nuclear magnetic dipoles in a resonator based on a coil with inductance L_C and resistance R_C is to be matched to a load R_L at the angular frequency ω_S of the MRI system using matching and tuning capacitors C_M and C_T. Generally, R_L should be matched to the series sum of R_C and the sample loading R_S. However, assuming that R_S is small (as shown experimentally later) and that the cable impedance Z_0 matches R_L, the system operates as shown in the simplified equivalent of Figure 2b.

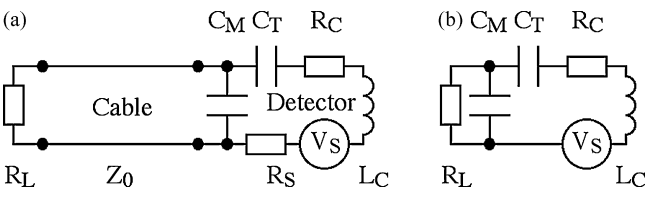

Figure 2. a) Electrical equivalent circuit and b) simplified equivalent.

Key to successful operation is development of impedance-matched cables and resonant detectors containing suitable matching circuits. Geometric constraints and the need for flexibility make it difficult to achieve the desired impedance using either a microstrip [33] or a coplanar waveguide [34]. Here we use a microstrip with a periodically patterned ground plane. This approach is commonly used in photonic bandgap devices [35], but it can also modify low-frequency impedance (a factor that was previously ignored in favour of filter applications). We use a simple resonant detector with integrated capacitors that can be fabricated using compatible processing, and demonstrate a convergent method of identifying the component values needed for matching and tuning. Combining these elements we demonstrate external ^{1}H magnetic resonance imaging at 1.5 T using a 2 metre-long catheter based detector, constructed entirely from thin film components.

A design for an impedance-matched thin-film cable is presented in Section 2, and fabrication and measurements of transmission characteristics in Section 3. A design for a compatible thin-film coil with integrated capacitors is presented in Section 4, and fabrication and matching and tuning are described in Section 5. Preliminary MRI experiments are described in Section 6 and conclusions are drawn in Section 7.

2. Thin-film cable design

In this Section, we consider possible cable formats, including microstrip, coplanar waveguide and periodically patterned microstrip, for an application such as a catheter-based MRI detector requiring very thin flexible layers of metals and dielectric.

2.1. Microstrip

Figure 3a shows one obvious possibility, a microstrip consisting of two conducting layers separated by an insulator of relative dielectric constant ε_r. One conducting layer is patterned into a strip of width w, and the thickness of conductor and insulator are t and h respectively. The characteristic impedance Z_0 can be estimated using Wheeler's formulae [33]:

$$Z_0 = Z_{FS}\, c_1 \log_e\{1 + c_2[c_2 c_3 + \sqrt{(c_2^2 c_3^2 + c_4)}]\} \quad (1)$$

Here $Z_{FS} = \sqrt{(\mu_0/\varepsilon_0)}$ is the impedance of free space, and:

$$c_1 = 1/\{2\pi\sqrt{[2(1+\varepsilon_r)]}\} \quad c_2 = 4h/w_{eff} \quad c_3 = (14 + 8/\varepsilon_r)/11 \quad c4 = \pi^2(1 + 1/\varepsilon_r)/2$$
$$w_{eff} = w + t\, c_5 \log_e\{4e/\sqrt{(c_6^2 + c_7^2)}\} \quad (2)$$
$$c_5 = (1 + 1/\varepsilon_r)/2\pi \quad c_6 = t/h \quad c_7 = 1/\{\pi(w/t + 11/10)\}^2$$

These expressions give the typical results shown in Figure 3a. Here, we have assumed t = 35 μm and ε_r = 3.5, to model a Cu-polyimide-Cu trilayer. Two curves are shown, for h = 25 μm and h = 50 μm, and 50 Ω impedance is only obtained for very small (< 100 μm) strip widths, with w reducing as h decreases. The explanation is the small separation of the conductors, which results in low inductance and high capacitance per unit length. Reliable lithographic fabrication in long lengths is therefore likely to be difficult. Larger inductance and/or smaller capacitance are required, but using moderate (w ≈ 1 mm) strip widths.

2.2. Coplanar waveguide

Figure 3b shows a second possibility, a coplanar waveguide (CPW) consisting of a ground-signal-ground arrangement on a dielectric backing. Z_0 is found by evaluating the capacitance C_p per

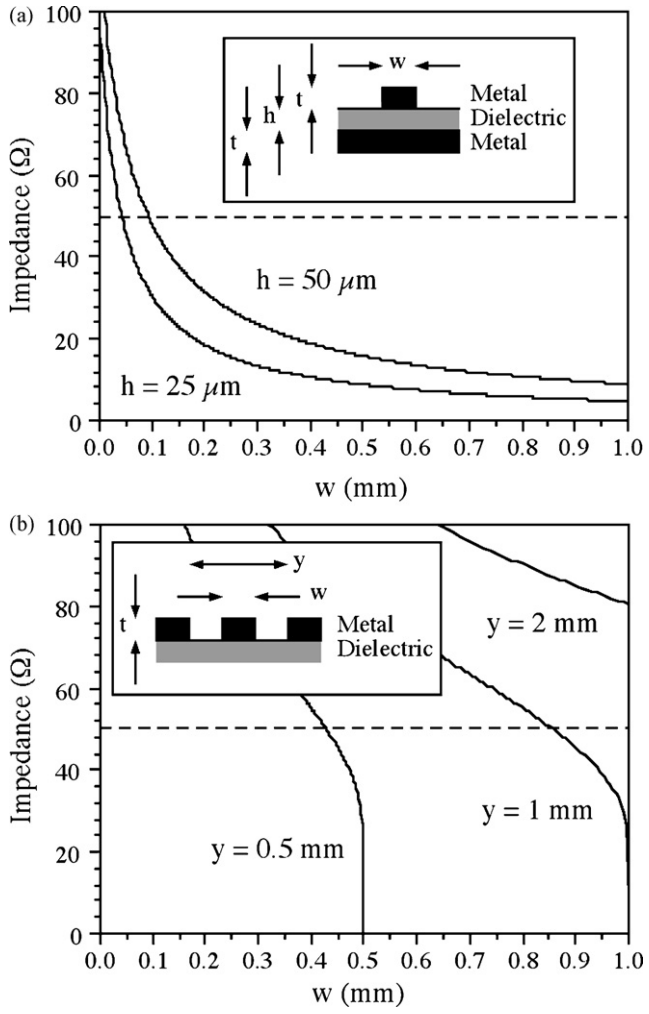

Figure 3. a) Variation of microstrip impedance with strip width w, for metal thickness t = 35 μm and different substrate thickness h; b) variation of coplanar waveguide impedance with strip width w, for different ground-plane separation y. In each case, $\varepsilon_r = 3.5$.

unit length by conformal mapping, and assuming that the effective dielectric constant is the average of that of the substrate and overlayer. If the latter is air, Wen's result is [34]:

$$Z_0 = 1/C_p v_{ph}, \quad where \quad v_{ph} = \{2/(\varepsilon_r + 1)\}^{1/2} c \quad \text{and} \quad C_p = (\varepsilon_r + 1)\varepsilon_0 2r \tag{3}$$

Here c is the velocity of light, r = K(k)/K'(k) and K(k) is a complete elliptic integral of the first kind with modulus k, such that:

$$K(k) = \int_0^{\pi/2} \{1 - k^2 \sin^2(\theta)\}^{-1/2} d\theta, \quad k = w/y, \quad K'(k) = K(k'),\ k' = (1 - k^2)^{1/2} \tag{4}$$

Figure 3b shows the variation of Z_0 with strip-width w for different values of the ground-plane separation y, again assuming that $\varepsilon_r = 3.5$. Although larger impedance may now be obtained using wider strips, 50 Ω is only reached when $w \approx 0.85\,y$. The explanation is the much smaller capacitance obtained in a CPW. Consequently, this geometry requires small electrode gaps, which are again hard to manufacture. Furthermore, C_P is now sensitive to the dielectric constant of the overlayer, which may vary significantly in practice.

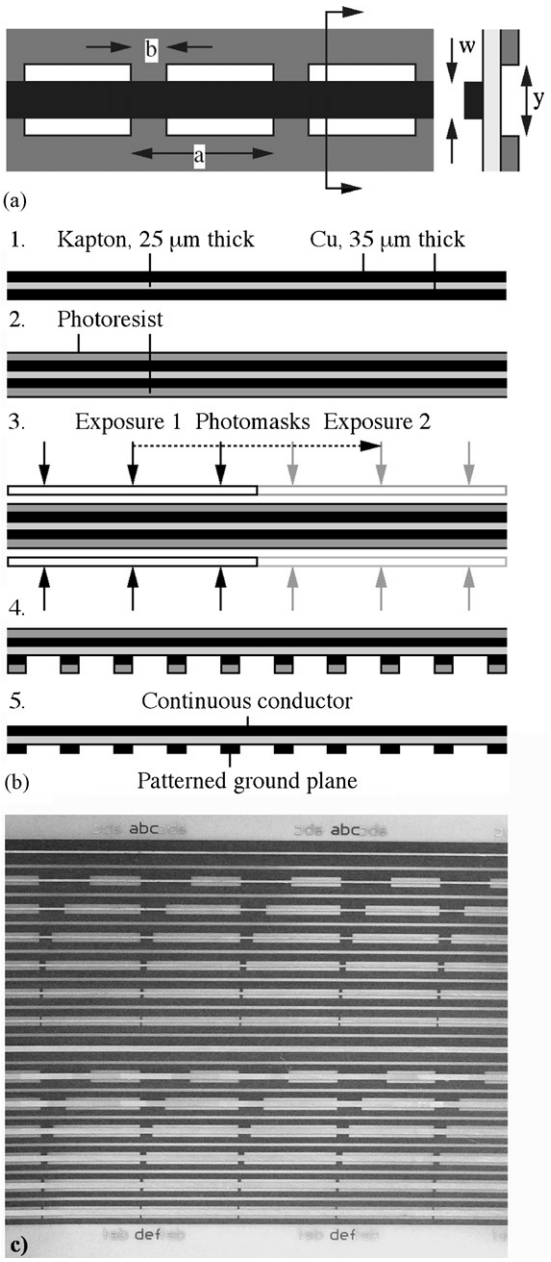

Figure 4. a) Layout of thin-film cable, b) process flow and b) completed cable array.

2.3. Periodically patterned microstrip

Figure 4a shows a third possibility, a modified microstrip whose ground plane is patterned with periodic openings that remove metal symmetrically to balance any externally induced voltages. The large separation between conductors in the open regions should increase average inductance and decrease average capacitance, allowing impedance to be controlled by the ratio b/a, where a is the period and b is the length of the regions where conductors overlap. The capacitance is now mainly defined in the overlap regions, stabilising the impedance against variations in its surroundings. A further possibility, where the top and bottom conductors are both meandered allows serial balancing of voltages.

Here, we focus on the geometry of Figure 4a. Strictly, this line is a bi-periodic structure, with different inductance and capacitance in alternating sections, and will generally have two propagating bands. However, if the period is sufficiently small and the component values in each section sufficiently different, the upper (optical)

branch will be at very high frequency. In estimating low-frequency behaviour, we may therefore ignore this branch. We simply assume that the impedance is dominated by an inductance L where the ground plane is cut away and a capacitance C where it remains. Behaviour in the lower (acoustic) branch is then well approximated by the standard dispersion relation of an L-C ladder:

$$\omega/\omega_0 = 2\sin(ka/2) \quad (5)$$

Here ω is the angular frequency, $\omega_0 = 1/\sqrt{(LC)}$, k is now the propagation constant and a is the period in Figure 4a. Propagation can take place from DC to a maximum frequency $f_m = \omega_0/\pi$ when $ka = \pi$. In this regime, the impedance is:

$$Z_0 = Z_0' \exp(jka/2) \quad (6)$$

Z_0 is complex, but tends to the real value $Z_0' = \sqrt{(L/C)}$ at low frequency. The standard result $S_{11} = (R_L - Z_0)/(R_L + Z_0)$ can then be used to predict the scattering at a junction with a load R_L. Good matching is achieved at DC as Z_0'/R_L tends to unity. However, the matching degrades as the frequency rises, and all the power is reflected at f_m, when Z_0 is purely imaginary.

Suitable design rules may be developed as follows. Using the geometric parameters in Figure 4a, the DC impedance may be written as:

$$Z_0' = \sqrt{\{(a-b)L_p/bC_p)\}} \quad (7)$$

Here L_p and C_p are values per unit length (p.u.l.) without the structuring. Similarly, ω_m can be written as:

$$\omega_m = 2/\sqrt{\{(a-b)L_p bC_p)\}} \quad (8)$$

Low-frequency matching to R_L will be achieved if $(a - b)L_p = R_L{}^2 bC_p$. An impedance-matched line will therefore have $\omega_m = 2/(R_L bC_p)$. To obtain reasonably constant impedance, operation might be restricted to frequencies below a given fraction of the cut-off frequency–say, $f < f_m/40$. The maximum allowed length b of capacitance per section is then:

$$b = 1/(40\pi f R_L C_p) \quad (9)$$

The overall period may then be found from the inductance L_p p.u.l. as:

$$a = b\{1 + R_L^2 C_p/L_p\} \quad (10)$$

Numerical parameters can then be found as follows. For C_P, the geometry suggests that a parallel plate model may be used. For w = 1 mm, h = 25 μm and $\varepsilon_r = 3.5$, $C_P \approx 1.24$ pF/mm. At 63.8 MHz we then obtain $f_m = 2.55$ GHz and b = 2 mm. Estimation of L_P is harder, since the inner conductor is a strip and the outer conductors are sheets whose shapes will modify on a catheter. However, if these details are ignored, the arrangement has a strong similarity to a CPW. We may therefore use Equations 3 and 4 to estimate the capacitance in the open areas, and then find the per-unit-length inductance as $L_p = Z_0{}'^2 C_p$. For y = 2 mm, w = 1 mm and $\varepsilon_r = 3.5$, we obtain $L_p \approx 0.4$ nH/mm. Assuming that $R_L = 50\,\Omega$, the period can then be found as a = 18 mm. These considerations suggest that centimetric periods and b/a ratios of around 1/8 will be suitable. In any case, re-arrangement of earlier results gives:

$$C_p = 2/(b\pi f_m Z_0'), \quad L_p = \{b/(a-b)\}C_p Z_0'^2 \quad (11)$$

Actual values of C_p and L_p may therefore be extracted from experimental measurement of the DC impedance Z_0' and the cut-off frequency f_m.

3. Thin-film cable fabrication and testing

In this Section we consider the fabrication of thin-film cables in sufficiently long lengths for internal imaging and carry out an initial electrical performance evaluation.

3.1. Cable fabrication

Side-viewing flexible gastroscopes for delivery of catheter tools into the bile duct have lengths > 1 m, and operate with catheters of ≈ 2 m length. Surface processing of flexible materials with such dimensions is beyond the scope of semiconductor techniques, but within the capability of PCB manufacture. Prototype cables were therefore fabricated in 2 m lengths by the flexible PCB company Clarydon (Willenhall, West Midlands, UK). The starting material was 25 μm thick polyimide (Kapton® HN, DuPont High Performance Films, Circleville, OH) carrying a 35 μm thick layer of Cu on either side. These dimensions yielded very flexible cable. Experiments were also carried out using thicker (50 μm) Kapton® but this yielded stiffer cables that required very thick heat-shrink for retention. Conversely, thinner (13 μm) Kapton® was difficult to handle in large sheets.

Patterning was carried out using stepped double-sided exposure to a pair of 1-metre long photomasks formed from Mylar-coated silver halide on a 175 μm thick polyester backing. Masks were fabricated from a Gerber file defining cables with different layouts. A period close to the previous estimate was used (a = 16 mm) so that each line contained 125 periods. The widths of the ground plane and its openings were 4 mm and 2 mm, respectively. A strip width of w = 1 mm was used, together with seven values of the ratio b/a (1, 1/2, 1/4, 1/8, 1/16, 1/32 and 1/64). The first corresponds to uniform microstrip and the others to periodic lines. Using standard panel widths the batch quantity was 24.

Figure 4b shows the fabrication process. Each side of the PCB (1) was first coated with a 175 μm thick layer of laminated photoresist (2). The sensitised PCB was then sandwiched between the two photomasks on a glass backing, using a set of pins passing through mating holes in each component for alignment. Textured Mylar spacers were used to assist evacuation during vacuum contact. Each side of the PCB was exposed with an UV lamp, and the process was repeated in a second exposure (3). Resist development and metal etching were carried out with the PCB horizontal, using a leader board to allow dragging through a spray developer and a spray etcher (4). The resist was then stripped (5). Lines were fabricated in arrays as shown in Figure 4c and separated using a scalpel.

3.2. Cable performance

Electrical performance was assessed using an electronic network analyser. Similar performance trends were obtained before and after mounting on a catheter, with any changes being attributable to a reduction in the inductance of patterned lines after being wrapped round a cylindrical former. Catheter-mounted lines were stable and could be flexed without significant variation in S-parameters. Uniform microstrip had very low impedance, as expected. Variants with periodically patterned ground planes offered significantly better matching at low frequency. Matching improved as the ratio b/a decreased until an optimum was reached, and a further reduction in b/a then degraded matching. For h = 25 μm and w = 1 mm, the optimum value was b/a = 1/8, in agreement with earlier estimates.

Figure 5a and b compare the frequency variation of S_{11} and S_{21}, respectively, for uniform microstrip and the optimum periodic cable. Here the measurements are taken up to the GHz regime to show the cut-off frequency. For the uniform microstrip, the reflection is high and oscillations in S_{11} and S_{21} can be seen at low frequency due to multiple reflections. At high frequencies (300 MHz), when losses are high enough that multiple reflections can be ignored, the return is $S_{11} \approx -1.9$ dB. The characteristic impedance may be estimated as 5.5 Ω. This value is in good agreement with a value of 4.5 Ω extracted from Figure 3a.

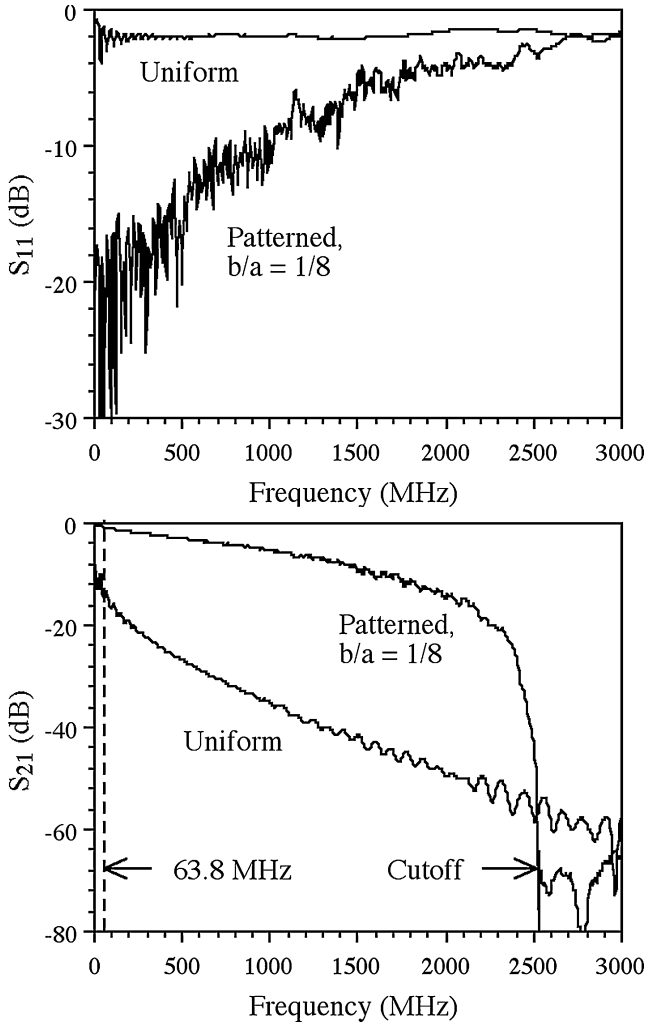

Figure 5. Experimental frequency variation of a) S_{11} and b) S_{21}, for uniform microstrip and for microstrip with a periodically patterned ground plane.

For the periodic cable, S_{11} is much lower at low frequencies, with a peak value below -15 dB up to 500 MHz, rising almost to 0 dB at the cutoff frequency, at which point the transmission S_{21} falls. The optical band was not observed at the limit of network analyser performance (8.5 GHz), suggesting that this must lie at very high frequencies. The capacitance and inductance per unit length were estimated from the DC impedance (45 Ω) and the cut-off frequency (2.5 GHz) as 2.8 pF/mm and 0.8 nH/mm, respectively, in reasonable agreement with earlier estimates. The characteristic impedance at 64 MHz is almost exactly the same as the value at DC, since this frequency is only 2.6% of the cutoff value and the impedance is almost constant in this range.

In addition to providing improved impedance matching, periodically patterned microstrip offers lower propagation loss than uniform microstrip. For example, the periodic cable in Figure 5b has low-frequency loss as low as 2.5 dB $GHz^{-1}m^{-1}$, making the losses negligible at 63.8 MHz. The combined effect of impedance matching and loss reduction is to increase throughput at MR frequencies by ≈15 dB compared with uniform microstrip.

4. Thin-film RF detector design

In this Section we consider the problem of designing a matched and tuned integrated resonant RF detector, in a format compatible with a thin-film cable.

4.1. RF detector design

Interfaces for conventional RF detectors are well understood. In Figure 2b, the signal induced by external nuclear dipoles is to be matched to a real load R_L at angular frequency ω_S using the capacitors C_M and C_T. The complex impedance of the parallel combination of R_L and C_M is $(1/j\omega C_M)\{1/(1 + 1/j\omega C_M R_L)\}$. If $\omega C_M R_L \gg 1$, this result may be approximated as $1/j\omega C_M + R'$ where $R_L' = 1/(\omega^2 C_M^2 R_L)$. The matching capacitor therefore effectively inserts a scaled, frequency dependent load into the resonator. The total impedance around the signal loop is then $R_C + R_L' + \{1/j\omega C_T + 1/j\omega C_M + j\omega L_C\}$. Matching involves choosing C_M so that $R_L' = R_C$ at the signal frequency, which requires:

$$C_M = 1/\{\omega_S \sqrt{(R_C R_L)}\} \tag{12}$$

Similarly, tuning involves choosing C_T so that the circuit is resonant at the signal frequency, which requires that the effective capacitance C_{eff} satisfy:

$$1/C_{eff} = 1/C_M + 1/C_T = \omega_S^2 L_C \tag{13}$$

Generally these conditions can be satisfied, and the values of C_M and C_T found by iteration. The latter is typically smaller for high-Q resonators. However, determination of C_M and C_T requires knowledge of R_C and L_C, and both can vary considerably without well-controlled fabrication.

Figure 1a shows the arrangement of the resonant RF detector, which provides a shunt matching circuit. Here, a spiral inductor is connected to two capacitors, which each use the substrate as an interlayer dielectric. Since no air-bridge is needed to exit the spiral, the entire layout may be fabricated simply from patterned conductors. A similar arrangement cannot be devised for the alternative series matching circuit, because this requires at least one via. The front side pattern consists of a spiral linked to two plates, while the rear side pattern consists of a pair of plates linked directly together. This layout places the matching capacitor C_M outside the coil, allowing direct connection to the cable, and the smaller tuning capacitor C_T inside. Double-sided processing is required, but front-to-back alignment is not critical since the capacitor plates need only overlap. With well-defined substrate and conductor thickness, the values of L_C, R_C, C_M and C_T are stable.

5. Thin-film RF detector fabrication and testing

In this Section we describe the fabrication of thin-film detectors, a method for identifying component values for matching and tuning, and construction of a catheter based probe.

5.1. RF detector fabrication

Coils were designed for ^{1}H MRI at 1.5 T, with the following parameters: conductor width 200 μm, conductor separation 100 μm, coil length 60 mm, and coil width 4.2 mm. The last value was chosen to place the long conductors on the diameter of an 8 Fr (2.7 mm dia) catheter. There would be little difficulty in scaling the coil dimensions to match a smaller catheter diameter, e.g. 5 Fr (1.7 mm dia), albeit at a cost of a reduction in field-of-view. However, the inductance would decrease slightly, so that physically larger capacitors would be needed to operate at a similar frequency. The Q-factor would also fall slightly, impacting on the achievable signal-to-noise ratio.

A major difficulty is that L_C and R_C must be known before C_M and C_T can be chosen, and hence before photomasks can be designed. To avoid expensive iteration, a three-stage approach was used. A set of inductors was first fabricated without capacitors (Batch 1), but with bond-pads to allow addition of a wire-bond air-bridge

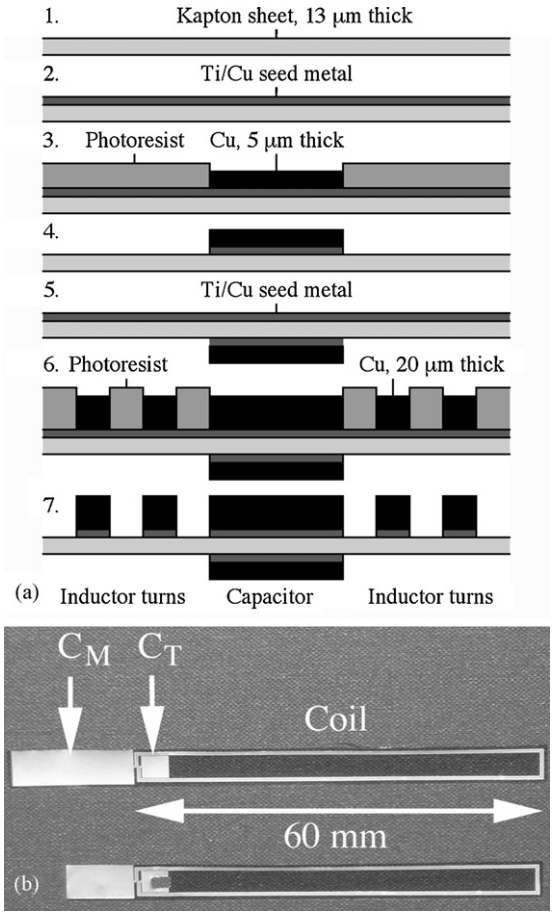

Figure 6. a) Process flow for detector fabrication, b) overall view of detectors, before (upper) and after (lower) capacitor trimming.

and surface-mount capacitors, which were adjusted to match to 50 Ω and tune to 63.8 MHz. A second set of devices was then fabricated with integrated capacitors (Batch 2), using areas for C_M and C_T estimated from Batch 1. The capacitors were trimmed to match and tune with a fixed tissue loading, and a final set of devices was fabricated using the known areas (Batch 3).

To reduce cost, RF detectors were fabricated separately from cables, using clean-room processes, and thinner (13 μm) Kapton® was used to reduce capacitor areas. Single-sided processing was used for coils, and double sided-processing for complete detectors. Figure 6a shows the process for detectors. The starting point was a Kapton® sheet, which was stretched over a 100 mm diameter silicon wafer to provide a rigid surface for processing (1). The rear-side capacitor plates were formed first. Seed layers of Ti (30 nm) and Cu (200 nm) were deposited by RF sputtering (2). A layer of AZ 9260 positive resist (Microchemicals GmbH, Ulm, Germany) was deposited by spin coating, and patterned using UV contact lithography to form a mould. 5 μm thick Cu conductors were then formed by electroplating, using Technic FB Bright Acid copper plating solution (Lektrachem Ltd., Nuneaton, UK) (3). The mould was stripped and exposed seed layer removed (4). The front-side capacitor plates and inductor were then formed. The sheet was detached from the wafer, turned over and replaced. The steps of seed metal deposition (5), mould formation and plating (6) and mould and seed layer removal (7) were then repeated, this time to form a 20 μm Cu layer. Figure 6b shows detectors from Batch 2, before and after tuning of capacitor areas.

5.2. Matching and tuning

Matching and tuning of Batch 1 detectors was carried out with the coil loosely attached to a catheter with heat shrink tubing. The additional capacitors were located just beyond the end of the catheter, and a sub-miniature co-axial cable was connected across C_M. Matching and tuning were achieved by minimising S_{11} at 63.8 MHz., with C_M = 139 pF and C_T = 19.5 pF. Ignoring self-capacitance, these values imply a total capacitance of C_{eff} = 17.1 pF, a coil inductance of $L_C = 1/(\omega_0^2 C_{eff}) = 0.36$ μH and a coil resistance of $R_C = 1/(\omega_0^2 C_M^2 R_L) = 6.4\,\Omega$ (and hence a quality factor of $Q = \omega_0 L_C/R_C = 23$). Batch 2 integrated resonators were fabricated using capacitor values approximately double those above. Devices were matched and tuned as before, adjusting capacitor areas using a scalpel. The final areas of C_M and C_T were 52 mm^2 and 9.3 mm^2, corresponding to 127 pF and 23 pF. The Q factor was estimated as 23, implying good performance from the integrated capacitors.

Tissue loading was then investigated by inserting a detector into butchered lamb's liver, which has a similar architecture to human liver. Loading caused a reduction in resonant frequency of ≈ 2 MHz, mainly due to an increase in self-capacitance of the multi-turn inductor caused by the change in dielectric surround, and a reduction in Q-factor from ca 23 to ca 20 due to the tissue conductivity. The latter result suggests that the sample loading is relatively small. Similar results were obtained using an agar gel phantom with a salt content chosen to mimic the conductivity and relaxation time of more general tissue (1% agar, 0.3% NaCl, 0.125% hydrated $CuSO_4$), suggesting that a common tuning condition can be used. The process above was then repeated to yield a device that tuned correctly after loading with tissue, and a final set of devices was fabricated using the known capacitor areas. These Batch 3 detectors required no adjustment.

5.3. Catheter probe assembly and performance

Catheter probes were constructed as follows. A slit was cut just to one side of the strip conductor in the cable. The detector was inserted into this slit and a soldered joint was made to the plates of the matching capacitor. The assembly was then fed through 150 μm thick biocompatible polyolefin heat-shrink tubing using a leader, and the tubing was in turn fed over the catheter. Finally the tubing was heated with cable and tube under tension, moving the heated zone to avoid trapped air. Figure 7a shows a completed detector and a section of cable.

Assembled probes functioned as expected. Figure 7b shows the frequency variation of the reflection coefficient S_{11} before (unloaded) and after (loaded) insertion in liver tissue, demonstrating that the coil tunes correctly to ca 64 MHz. Also shown are the corresponding variations of the transmission coefficient S_{21}, obtained using a small loop outside the tissue as a signal source. The degradation in Q-factor caused by loading is small, suggesting that coil loss is dominant over tissue loss and validating the assumptions of Figure 2.

The stability of the resonant frequency and of the Q-factor could be further improved, by mounting the coil on a catheter with reduced diameter using an increased thickness of heat shrink tubing. However, the received signal and signal-to-noise ratio (and hence the useful resolution and field of view) would then degrade, due to the reduced sample loading [36,37]. Clearly, a design optimisation along the lines of those carried out for surface coils [38,39] and for other internal coils [40,41] is an important future goal.

The thin film cable did however provide less effective shielding than conventional cable. Pickup was investigated by placing a small loop transmitter first near the detector and then near the adjacent cable, in each case adjusting the loop position to maximise coupling. The thick lines in Figure 8a shows the frequency variation of the sig-

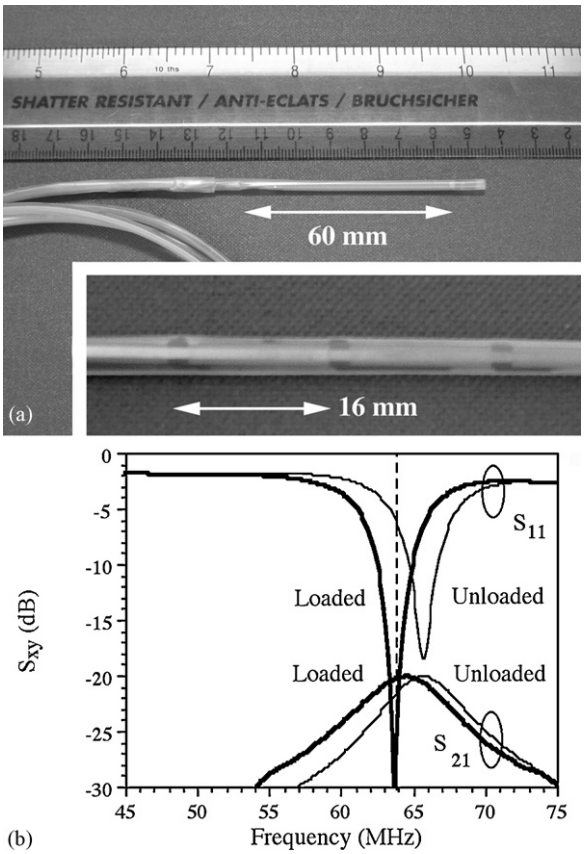

Figure 7. a) Catheter-based detector (main) and cable (inset); b) frequency variation of S_{11} and S_{21} unloaded (thin lines) and loaded by insertion into liver (thick lines).

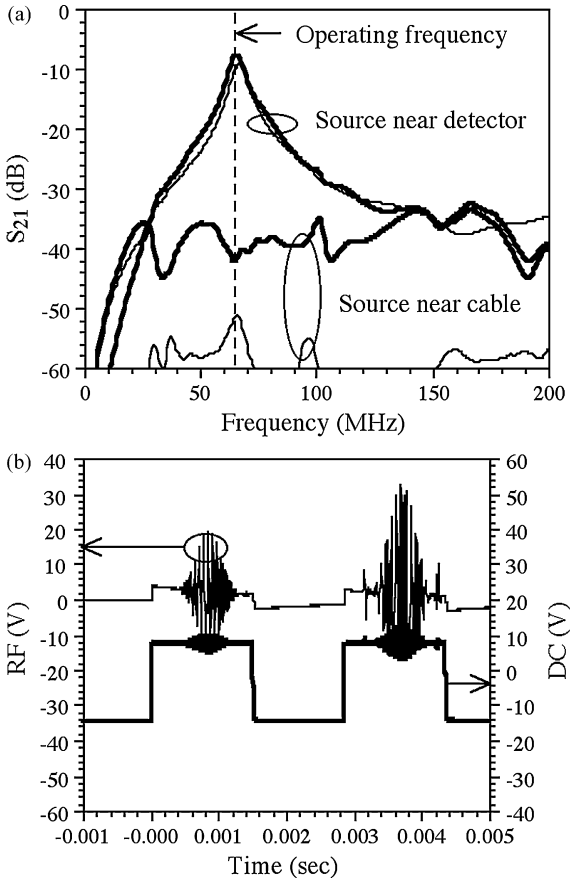

Figure 8. a) Experimental frequency variation of detected signal, with inductive source next to detector and cable. Thick and thin lines show results using i) thin film and ii) co-axial output, respectively. b) RF and DC control signals detected during manual pre-scan before ^{1}H MRI.

nal in each case. Near the operating frequency, the signal detected by the coil is ≈ 30 dB higher than the signal coupled into the cable. The experiment was then repeated using a second detector constructed using a co-axial output. The thin lines in Figure 8a show the corresponding results. While the performances of the detectors are essentially identical, the noise rejection by the co-axial cable is ≈ 20 dB greater.

6. Magnetic resonance imaging

In this Section, we present preliminary results for ^{1}H internal MRI, using *in vitro* tissue.

6.1. Imaging set-up

^{1}H magnetic resonance imaging was carried out using a 1.5 T GE HD Signa® Excite® scanner at St. Mary's Hospital, Paddington. The system body coil was used for transmission and a catheter probe was connected to an auxiliary coil input for reception. This input is normally used with surface coils such as shoulder coils and provides additional DC signals to control PIN diode switched decoupling. However, such precautions were not initially used to prevent direct magnetic coupling of the detector to the transmitter. The catheter was arranged parallel to the magnet bore, with the coil conductors lying in the coronal plane. The probe was placed either on or inside the imaging subject, which in turn lay on the patient bed. The bed was then translated to place the coil at the magnet isocentre. The coil would clearly be insensitive to MR signals with its plane perpendicular to the magnet bore. During an internal procedure such as biliary imaging, the patient would ideally be arranged to avoid this orientation. Further work is clearly required to evaluate any anatomical restrictions, which might require development of a thin-film coil with an alternative field of view.

Imaging was carried out using a 3D FRFSE (fast recovery, fast spin echo) sequence with an excitation time (TE) of 15 msec and a repetition time (TR) of 33 msec. The flip angle (10°) was the value set by the scanner itself, during an auto-prescan routine carried out using the body coil. Images were acquired in a block of 28 slices using, using 6 excitations to improve signal-to-noise ratio, in a total acquisition time of 11 min 53 sec. The field of view was 80 mm x 40 mm (for sagittal images) and 100 mm x 50 mm (for axial images) and the slice thickness and slice separation were each 1.2 mm. The data were reconstructed into images containing 256 × 256 pixels. These parameters correspond to voxel sizes of 0.3125 × 0.3125 × 1.2 mm^3 (sagittal) and 0.3096 × 0.3096 × 1.2 mm^3 (axial).

6.2. Initial characterisation

Initial experiments were carried out to assess the peak value of any magnetically induced voltages, and their likely effect on coil lifetime. A RF 'tee' was connected between the catheter coil and the scanner input, and the RF and DC control signals were taken to separate channels on a monitoring oscilloscope. Figure 8b shows a typical time variation of both signals. There is some breakthrough of RF on the control signal, and vice versa. The DC PIN diode control signal is high during the excitation phase of MRI, allowing the scope to be triggered easily and this phase to be identified. During excitation, RF signals of several tens of volts are detected across C_M. Signals across C_T would be correspondingly larger, due to its smaller size. Despite this, such coils have routinely

survived imaging experiments lasting several hours, except when using alternative sequences involving higher average RF powers. In this case, failure has typically occurred after minutes of acquisition. Subsequent investigation has suggested dielectric breakdown of the polyimide interlayer rather than conductor melting as the cause of failure.

6.3. Phantom imaging

Imaging experiments were then carried out with the catheter probe completely immersed in an agar gel phantom. The same imaging sequence was used, again setting transmit power using the auto pre-scan facility. The flip angle was therefore the nominal value determined in this process; however, resonant detection of the transmitted signal would be expected to modify the excitation pattern near the catheter coil significantly, causing flip angles to vary locally from the desired value. Images obtained from the body coil showed that the catheter coil did indeed distort the excitation uniformity. Because of the small flip angle used, the distortion was typically seen as an extremely bright concentric ring around the catheter, surrounded by a darker ring and then by a gradual radial decay.

Further experiments were carried out using a similar coil, fitted with PIN-diode switched decoupling based on a sub-miniature co-axial output cable. In this case, a slight reduction in Q-factor and a small change in resonant frequency were observed, requiring alterations to the matching and tuning conditions. Considerably improved image uniformity was obtained, confirming the need for effective decoupling. However, due to the difficulties involved in incorporating relatively bulky PIN diodes in a thin-film structure, an alternative approach such as the use of a figure-of-eight coil is planned for future investigation.

6.4. In vitro imaging

In vitro imaging was demonstrated using a butchered lamb's liver. The catheter probe was inserted into an accessible biliary duct, and the liver was then positioned to place the coil in a similar location and orientation inside the magnet. Transmit power was again adjusted using the auto pre-scan facility.

Figure 9a shows a sagittal slice passing through the bile duct, which lies near the surface. The liver occupies the right hand three-quarters of the image, which has been cropped to 50 mm field-of-view to emphasise detail. The catheter track can be seen as a pair of bright lines originating from the over-excitation described earlier, and an adjacent duct can be seen nearby. Generally uniform brightness is obtained over at least 4 cm parallel to the catheter track.

Figure 9b shows an axial slice transverse to the duct. Here the liver occupies the lower two-thirds of the image, which has again been cropped. The bile duct itself is at the centre of the image, with the central dark area defining the catheter location. The useful field of view of the coil is a co-axial cylinder of around 15 mm diameter. Despite the tissue loading, a signal-to-noise ratio of 75 is obtained in the immediate vicinity of the coil, reducing to around 35 averaged over the coil FOV. An adjacent duct may again be seen, and the wall of this duct, which has a thickness of around 0.5 mm, may be identified as a concentric band that is not associated with any distortion of the excitation.

This result suggests sub-millimetre resolution and implies the future possibility of detecting tumours that cause variations in thickness of the bile duct wall, or breaching of the duct wall integrity with invasion into surrounding tissue. The voxel size and signal-to-noise ratio achievable during *in vivo* imaging are likely to be limited by motion artefacts. However, the imaging conditions used here suggest that similar resolution and SNR could be obtained over a reduced number of slices (say, 3) in just over a minute, well within the possibility of breath holding.

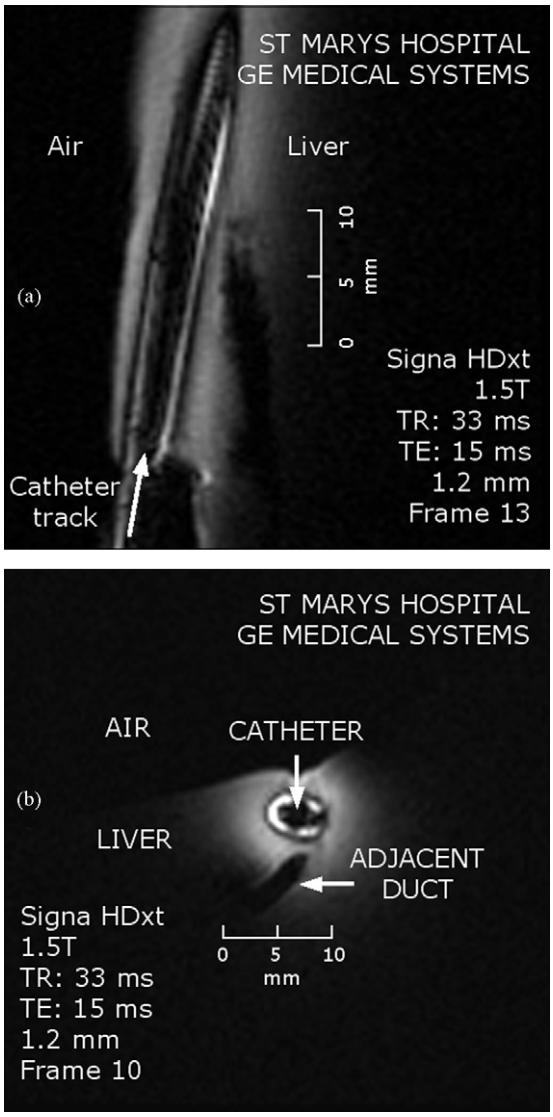

Figure 9. ^{1}H MR images of liver duct with coil inserted into butchered lamb's liver: a) sagittal, and b) axial.

7. Discussion

We have demonstrated a RF detector designed for internal MRI, based on a thin film resonator and a compatible cable. In each case, fabrication was carried out using double-sided processing of a Cu-Kapton-Cu trilayer to yield a flexible strip designed for attachment to a catheter. Although two different substrates were used, the arrangement is suitable for full integration. In fact, we have already demonstrated resonant detectors using the PCB process for cables. The detectors were stiffer due to the increased (25 μm) Kapton® thickness but had an improved unloaded Q factor (50) due to the increased (35 μm) Cu thickness. The components may be integrated onto catheters without altering their functionality, to provide a low-cost system for internal MRI or MR-guided procedures.

Here, we have focused mainly on impedance matching. There is scope for further miniaturisation, and for increasing high-frequency performance using smaller cable periods. However, further modifications are required before *in vivo* use, to protect against direct coupling to the magnetic or electric field of the trans-

mitter. To avoid a DC path, crossed diode pairs are commonly used to de-tune receivers passively during excitation [42]. However, as previously suggested, a printable solution such as a figure-of-eight coil may be preferable. Similarly, cables are subdivided with transformers into segments shorter than the resonant length [43], and a thin-film embodiment of such cable has already been demonstrated [44]. Although these issues may be less important using an endoscope, patient safety should clearly be paramount. Work is in therefore in progress to incorporate suitable features.

Acknowledgements

The authors are extremely grateful to EPSRC for support under grant EP/E005888/1 "*In vivo* biliary imaging and tissue sampling", to John Barry of Clarydon for the manufacture of flexible PCBs, and Prof. Wady Gedroyc for access to the 1.5 T scanner. CAW and SDT-R are grateful to the NIHR Biomedical Facility at Imperial for infrastructure support.

References

[1] G.C. Hurst, G.J. Misic, Coils for insertion into the human body, in: D.M. Grant, R.K. Harris (Eds.), Encyclopedia of nuclear magnetic resonance, John Wiley and Sons, Chichester, 1996, pp. 1373–1378.
[2] H.L. Kantor, R.W. Briggs, R.S. Balaban, In vivo ^{31}P nuclear magnetic resonance measurements in canine heart using a catheter-coil, Circ. Res. 55 (1984) 261–266.
[3] S.G. Worthley, G. Helft, V. Fuster, Z.A. Fayad, M. Shinnar, L.A. Minkoff, C. Schecter, T.J. Fallon, J.J. Badimon, A novel nonobstructive intravascular MRI coil: in vivo imaging of experimental atherosclerosis, Arterioscler. Thromb. Vasc. Biol. 23 (2003) 346–350.
[4] M. Armenean, O. Beuf, F. Pilleul, H. Saint-Jalmes, Optimization of endoluminal loop radiofrequency coils for gastrointestinal wall MR imaging, IEEE Sensors J. 4 (2004) 57–64.
[5] E. Atalar, P.A. Bottomley, O. Ocali, L.C.L. Correia, M.D. Kelemen, J.A.C. Lima, E.A. Zerhouni, High resolution intravascular MRI and MRS by using a catheter receiver coil, Mag. Res. Med. 36 (1996) 596–605.
[6] P.J. Martin, D.B. Plewes, R.M. Henkelman, MR imaging of blood vessels with an intravascular coil, J. Mag. Res. Imag. 2 (1992) 421–429.
[7] G.C. Hurst, J. Hua, J.L. Duerk, A.M. Cohen, Intravascular (catheter) NMR receiver probe: preliminary design analysis and application to canine iliofemoral imaging, Mag. Res. Med. 24 (1992) 343–357.
[8] O. Ocali, E. Atalar, Intravascular magnetic resonance imaging using a loopless catheter antenna, Mag. Res. Med. 37 (1997) 112–118.
[9] C.L. Dumoulin, S.P. Souza, R.D. Darrow, Real-time position monitoring of invasive devices using magnetic resonance, Mag. Res. Med. 29 (1993) 411–415.
[10] S. Zuehlsdorff, R. Umathum, S. Volz, P. Hallscheidt, C. Fink, W. Semmler, M. Bock, MR coil design for simultaneous tip tracking and curvature delineation of a catheter, Mag. Res. Med. 52 (2004) 214–218.
[11] H.H. Quick, M.E. Ladd, G.G. Zimmermann-Paul, P. Erhart, E. Hofmann, G.K. von Schulthess, J.F. Debatin, Single-loop coil concepts for intravascular magnetic resonance imaging, Mag. Res. Med. 41 (1999) 751–758.
[12] T.L. Peck, R.L. Magin, J. Kruse, M. Feng, NMR microspectroscopy on 100-μm planar RF coils fabricated on gallium arsenide substrates, IEEE T. Biomed. Eng. 41 (1994) 706–709.
[13] J.E. Stocker, T.L. Peck, A.G. Webb, M. Feng, R.L. Magin, Nanoliter volume, high-resolution NMR microspectroscopy using a 60-μm planar microcoil, IEEE T, Biomed. Eng. 44 (1997) 1122–1127.
[14] L. Renaud, M. Armenean, L. Berry, P. Kleimann, P. Morin, M. Pitaval, J. O'Brien, M. Brunet, H. Saint-Jalmes, Implantable planar RF microcoils for NMR microspectroscopy, Sensors and Actuators A99 (2002) 244–248.
[15] R.R.A. Syms, M.M. Ahmad, I.R. Young, D.J. Gilderdale, D.J. Collins, Microengineered needle micro-coils for magnetic resonance spectroscopy, J. Micromech. Microeng. 16 (2006) 2755–2764.
[16] J. Dechow, A. Forchel, T. Lanz, A. Haase, Fabrication of NMR-microsensors for nanoliter sample volumes, Microelectr. Engng. 53 (2000) 517–519.
[17] C. Massin, C. Boero, F. Vincent, J. Abenhaim, P.A. Besse, R.S. Popovic, High-Q factor RF planar microcoils for micro-scale NMR spectroscopy, Sensors and Actuators A97-8 (2002) 280–288.
[18] R.R.A. Syms, M.M. Ahmad, I.R. Young, Y. Li, J. Hand, D. Gilderdale, MEMS Helmholtz coils for magnetic resonance imaging, J. Micromech. Microeng. 15 (2005) S1–S9.
[19] K. Ehrmann, N. Saillen, F. Vincent, M. Stettler, M. Jordan, F.W. Wurm, P.-A Besse, R. Popovic, Microfabricated solenoids and Helmholtz coils for NMR spectroscopy of mammalian cells, Lab Chip 7 (2007) 373–380.
[20] J.A. Rogers, R.J. Jackman, G.M. Whitesides, D.L. Olson, J.V. Sweedler, Using microcontact printing to fabricate microcoils on capillaries for high resolution proton nuclear magnetic resonance on nanoliter volumes, Appl. Phys. Lett. 70 (1997) 2464–2466.
[21] L. Berry, L. Renaud, P. Kleimann, P. Morin, M. Armenean, H. Saint-Jalmes, Development of implantable detection microcoils for minimally invasive NMR spectroscopy, Sensors and Actuators A93 (2001) 214–218.
[22] V. Malba, R. Maxwell, L.B. Evans, A. Bernhardt, M. Cosman, K. Yan, Laser-lathe lithography–a novel method for manufacturing nuclear magnetic resonance microcoils, Biomed. Microdev. 5 (2003) 21–27.
[23] J.D. Trumbull, I.K. Glasgow, D.J. Beebe, R.L. Magin, Integrating microfabricated fluidic systems and NMR spectroscopy, IEEE T. Biomed. Eng. 47 (2000) 3–7.
[24] C. Massin, F. Vincent, A. Homsy, K. Ehrmann, G. Boero, P.A. Besse, A. Daridon, E. Verpoorte, N.F. de Rooij, R.S. Popovic, Planar microcoil-based microfluidic NMR probes, J. Mag. Res. 164 (2003) 242–255.
[25] J.E. Stocker, T.L. Peck, S.J. Franke, J. Kruse, M. Feng, R.L. Magin, Development of an integrated detector for NMR microscopy, in: Proc. IEEE Engineering in Medicine and Biology Conf., Montreal, Canada, Sept. 20-25, 1995, pp. 843–844.
[26] G. Boero, J. Frounchi, B. Furrer, P.-A. Besse, R.S. Popovic, Fully integrated probe for proton nuclear magnetic resonance spectroscopy, Rev. Sci. Inst. 72 (2001) 2764–2768.
[27] J. Dechow, T. Lanz, M. Stumber, A. Forchel, A. Haase, Preamplified planar microcoil on GaAs substrates for microspectroscopy, Rev. Sci. Inst. 74 (2003) 4855–4857.
[28] A.-L. Coutrot, E. Dufour-Gergam, J.-M. Quemper, E. Martincic, J.-P. Gilles, J.P. Grandchamp, M. Matlosz, A. Sanchez, L. Darasse, J.-C. Ginefri, Copper micromolding process for NMR microinductors realisation, Sensors and Actuators A99 (2002) 49–54.
[29] S. Eroglu, B. Gimi, B. Roman, G. Friedman, R.L. Magin, NMR spiral surface microcoils: design, fabrication and imaging, Conc. Mag. Res. B 17 (2003) 1–10.
[30] D. Ellersiek, S. Harms, F. Casanova, B. Blümich, W. Mokwa, U. Schnakenberg, Flexible RF microcoils with integrated capacitor for NMR applications, in: Proc. MME'05, Göteborg, Sweden, Sept. 4-6, 2005, pp. 256–259.
[31] M. Woytaskik, J.-C. Ginefri, J.-S. Raynaud, M. Poirier-Wuinot, E. Dufour-Gergam, J.-P. Grandchamp, O. Girard, P. Robert, J.-P. Gilles, E. Martincic, L. Darasse, Characterisation of flexible RF microcoils dedicated to local MRI, Microsyst. Tech. 13 (2007) 1575–1580.
[32] M.M. Ahmad, R.R.A. Syms, I.R. Young, B. Mathew, W. Casperz, S.D. Taylor-Robinson, C.A. Wadsworth, W.M.W. Gedroyc, Catheter-based flexible microcoil RF detectors for internal magnetic resonance imaging, J. Micromech. Microeng. 19 (2009) 074011.
[33] H.A. Wheeler, Transmission-line properties of a strip on a dielectric sheet on a plane, IEEE Trans. Micr. Theory & Tech. MTT-25 (1977) 631–647.
[34] C.P. Wen, Coplanar waveguide: a surface strip transmission line suitable for nonreciprocal gyromagnetic device applications, IEEE Trans. Microwave Theory and Tech. MTT-17 (1969) 1087–1990.
[35] F. Falcone, T. Lopetegi, M. Sorolla, 1-D and 2-D photonic bandgap structures, Micr. Opt. Tech. Lett. 22 (1999) 411–412.
[36] D.I. Hoult, P.C. Lauterbur, The sensitivity of the zeugmatographic experiment involving human samples, J. Magn. Reson. 34 (1979) 425–433.
[37] J.M. Libove, J.R. Singer, Resolution and signal-to-noise relationships in NMR imaging in the human body, J. Phys. E. Sci. Inst. 13 (1980) 38–44.
[38] C.E. Hayes, L. Axel, Noise performance of surface coils for magnetic resonance imaging at 1.5 T, Med. Phys. 12 (1985) 604–607.
[39] M.D. Harpen, Sample noise with circular surface coils, Med. Phys. 14 (1987) 616–618.
[40] P.A. Bottomley, E. Atalar, R.F. Lee, K.A. Shunk, A. Lardo, Cardiovascular MRI probes for the outside in and for the inside out, Mag. Res. Mats. in Phys., Biol. and Med. 11 (2000) 49–51.
[41] H. Celik, Y. Eryaman, A. Altinas, I.A. Abdel-Hafez, E. Atalar, Evaluation of internal MRI coils using ultimate intrinsic SNR, Mag. Res. Med. 52 (2004) 640–649.
[42] M.R. Bendall, A. Connelly, J.M. McKendry, Elimination of coupling between cylindrical transmit coils and surface-receive coils for *in vivo* NMR, Mag. Res. Med. 3 (1986) 157–163.
[43] S. Weiss, P. Vernickel, T. Schaeffter, V. Schulz, B. Gleich, Transmission line for improved RF safety of interventional devices, Mag. Res. Med. 54 (2005) 182–189.
[44] R.R.A. Syms, I.R. Young, L. Solymar, T. Floume, Thin-film magneto-inductive waveguides, J. Phys. D. Appl. Phys. 43 (2010) 055102.

Biographies

Richard Syms has been Professor of Microsystems Technology at Imperial College London since 1996. He obtained a BA in Engineering Science in 1979 and a D.Phil. in 1982, both from Oxford University. He has carried out research on holography, integrated optics, laser and amplifier devices and microengineering, and most recently has been developing sensors such as miniature quadrupole mass spectrometers and RF probes for magnetic resonance imaging.

Ian Young has been a Senior Research Fellow and Visiting Professor at Imperial College London since 2001. Prior to that, he led the Physics and Engineering Group at the Robert Steiner MRI Unit at Hammersmith Hospital from its initiation until 1997. During this time, it was responsible for many of the features that are now commonplace worldwide. He has published over 300 papers, and has been granted in excess of 50 patents, the vast majority relating to the development of MRI and MRS.

Munir Ahmad has been a Senior Research Assistant at Imperial College London since 1993. He obtained a BSc in Physics and Chemistry 1967 and a MSc in Chemistry in

1970 from the University of the Punjab, and a PhD in Organic Semiconductors in 1978 from the University of Bradford. His current interests include microengineered components for magnetic resonance imaging and spectroscopy, and novel methods for nanofabrication.

Marc Rea is a clinical scientist at Imperial College NHS Trust, and has Masters degrees in Physics, Medical Physics and Computing. He has a PhD from Imperial College London, awarded in 2010. His current research interests include MR-compatible robotics, position tracking and MR imaging.

Chris Wadsworth is a Gastroenterology Specialist Registrar at St. Mary's Hospital, Paddington, London, UK and is a Clinical Research Fellow in the Department of Hepatology and Gastroenterology, Imperial College London, UK. He graduated in medicine, receiving MBBS degrees from St George's, University of London in 2001.

Current areas of research interest: Liver and bile duct cancers, ERCP and endoscopy

Simon Taylor-Robinson has been Professor of Translational Medicine at St. Mary's Hospital, Imperial College London since 2007. He obtained a MB BS in 1984 and a MD in 1996, both from the University of London. He heads the Translational Research Facility at St Mary's Hospital, which encompasses a metabonomic, genomic, proteomic and *in vivo* imaging research approach. His major research interests include pathogenic and biochemical mechanisms of liver injury in patients with cirrhosis and the pathogenesis of hepatic encephalopathy.